Supporting Information

Interfacing MnO and FeCo alloy inside N-doped carbon hierarchical porous nanospheres derived from metal-organic framework boosts high-performance oxygen reduction for Zn–air batteries

Xinde Duan[1], Minqi Xia[2], Xixi Hu[3], Lijun Yang[2] and Hegen Zheng[1*]

[1]State Key Laboratory of Coordination Chemistry, School of Chemistry and Chemical Engineering, Collaborative Innovation Center of Advanced Microstructures, Nanjing University, Nanjing 210023, PR China

[2]Key Laboratory of Mesoscopic Chemistry of MOE and Jiangsu Provincial Laboratory for Nanotechnology, School of Chemistry and Chemical Engineering, Nanjing University, Nanjing 210023, PR China

[3]Kuang Yaming Honors School, Institute for Brain Sciences, Nanjing University, Nanjing 210023, PR China
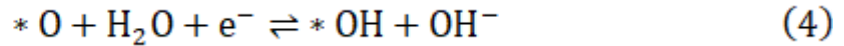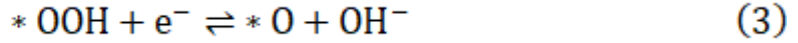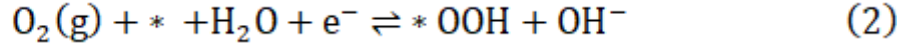
* Corresponding author

E-mail: zhenghg@nju.edu.cn

Reaction free energy calculation details

The ORR pathway was calculated according to the framework developed by Nørskov.[1] In an alkaline electrolyte (pH=13), the overall reaction can be written as:

$$O_2(g) + 2H_2O + 4e^- \rightleftharpoons 4OH^-(aq) \tag{1}$$
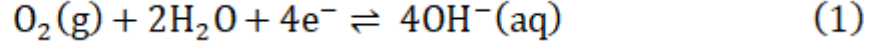
and the reaction proceeds through the following elementary steps:

$$O_2(g) + * + H_2O + e^- \rightleftharpoons *OOH + OH^- \tag{2}$$

$$*OOH + e^- \rightleftharpoons *O + OH^- \tag{3}$$

$$*O + H_2O + e^- \rightleftharpoons *OH + OH^- \tag{4}$$

$$*OH + e^- \rightleftharpoons * + OH^- \tag{5}$$

For each elementary step, the Gibbs reaction free energy ΔG is defined as:

$$\Delta G = \Delta E + \Delta ZPE - T\Delta S + \Delta G_U + \Delta G_{pH} \tag{6}$$

where ΔE is the energy difference between reactants and products, ΔZPE and ΔS are the change in zero point energies and entropy at temperature T. ΔG_U, which results from electron transferring under electrode potential, is calculated by:

$$\Delta G_U = -neU \tag{7}$$

where U is the applied electrode potential relative to SHE and n is the number of proton–electron pairs transferred. ΔG_{pH} is the correction of the H^+ free energy, which is calculated by:

$$\Delta G_{pH} = -k_B T \ln[H^+] = 0.0592 pH \tag{8}$$

where k_B is the Boltzmann constant. Hence, the equilibrium potential U_0 for ORR at pH=13 is determined to be 0.461V versus SHE.

As the free energy of oxygen molecule can not be described precisely in DFT, we derived $G_{O_2}(g)$ according to the equation:

$$G_{O_2}(g) = 2G_{H_2O}(l) - G_{H_2} + 4 \times 1.23 \text{ (eV)} \tag{9}$$

where the gas-phase H_2O at 0.035 bar was used as reference state to calculate $G_{H_2O}(l)$ at 298.15K. The free energy of OH^- was derived as:

$$G_{OH^-} = G_{H_2O}(l) - G_{H^+} \tag{10}$$

For ORR, the onset potential is calculated by:

$$U_{ORR}^{onset} = -\max\{\Delta G_1, \Delta G_2, \Delta G_3, \Delta G_4\} \tag{11}$$

where ΔG_1 to ΔG_4 corresponds to the reaction free energy of four elementary steps.
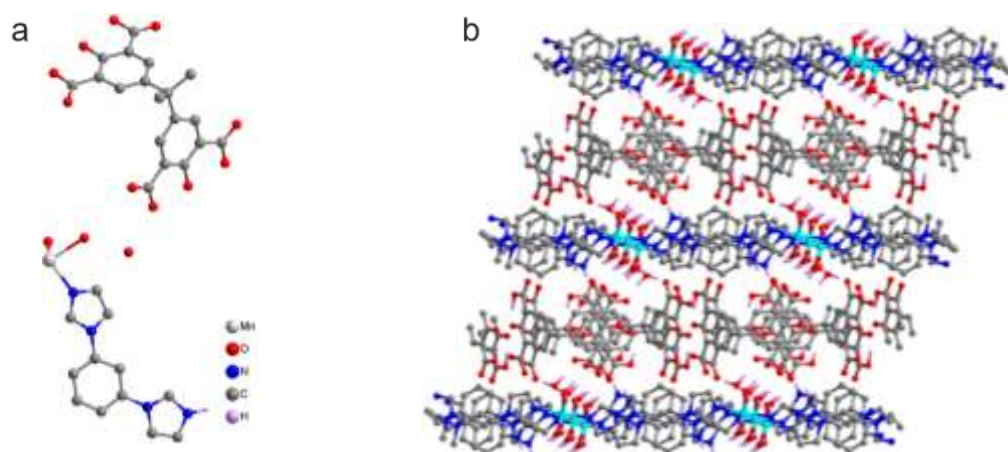

Figure S1. (a) The coordination modes of ligands and the coordination geometries of Mn^{2+} cations in Mn-MOF. (b) Views of accumulational architecture of Mn-MOF.
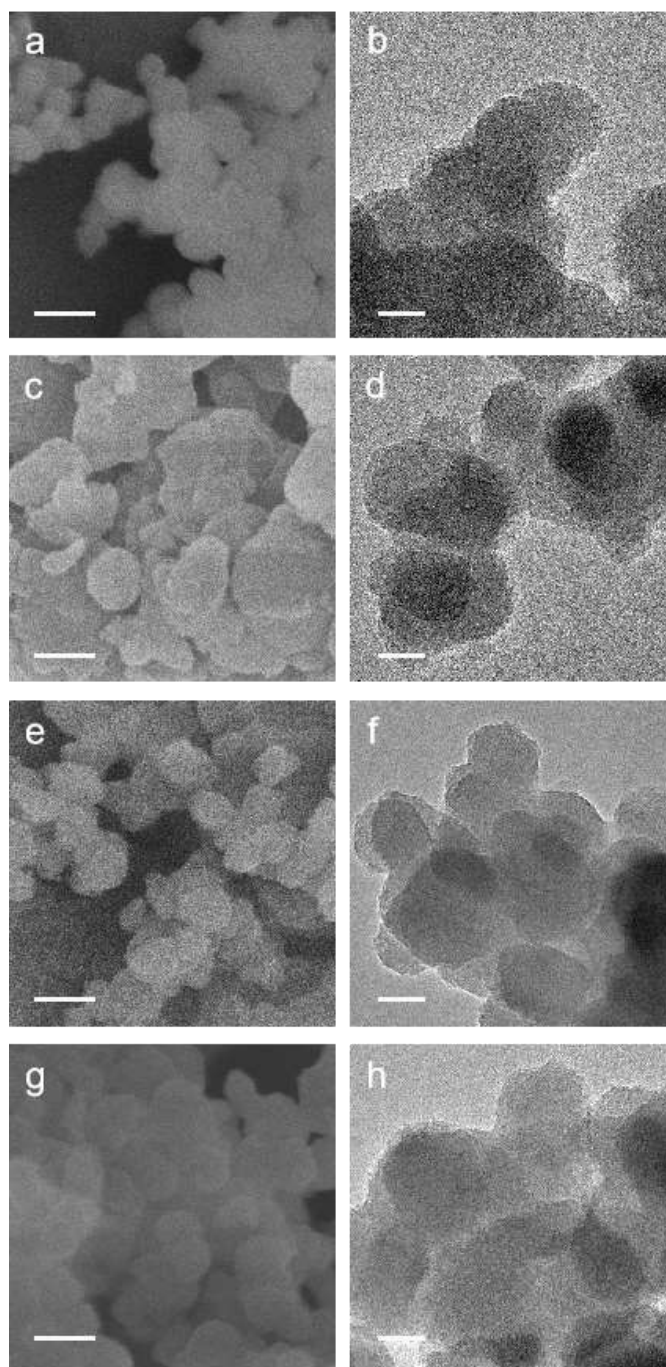
Figure S2. (a,c,e,g) SEM (200 nm) and (b,d,f,h) TEM (5 nm) images of (a,b) Mn-MOF, (c,d) Fe@Mn-MOF, (e,f) Co@Mn-MOF, and (g,h) CoFe@Mn-MOF.
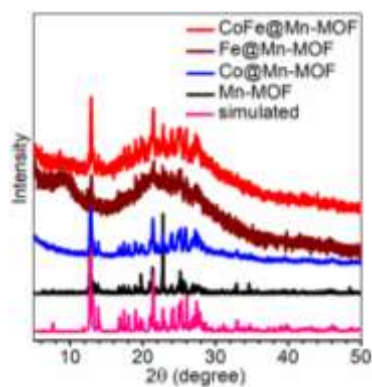
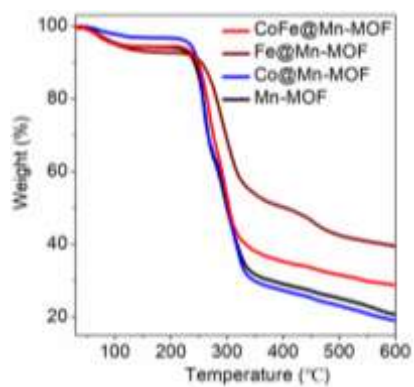**Figure S3.** PXRD patterns of Mn-MOF, Fe@Mn-MOF, Co@Mn-MOF, and CoFe@Mn-MOF.

Figure S4. Thermo-gravimetric plots of Mn-MOF, Fe@Mn-MOF, Co@Mn-MOF, and CoFe@Mn-MOF under N_2 from 25 to 600 °C with a heating rate of 10 °C min^{-1}.
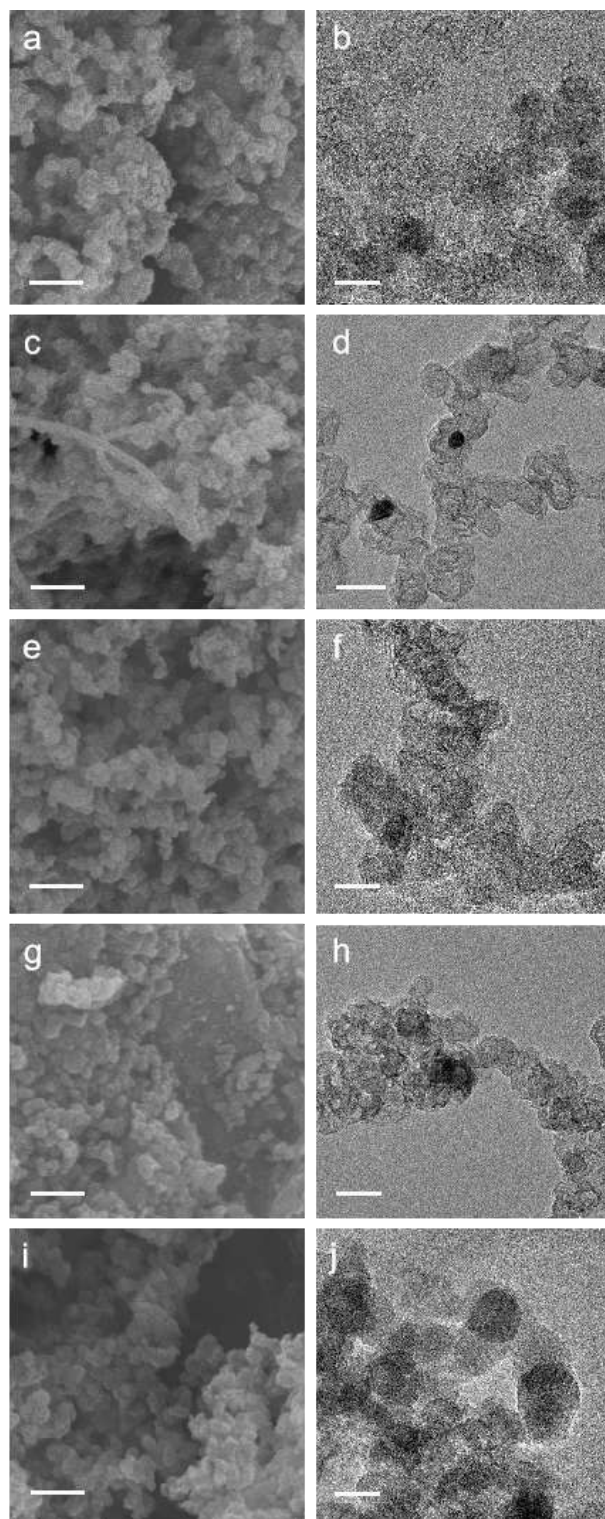
Figure S5. (a,c,e,g,i) SEM (200 nm) and (b,d,f,h,j) TEM (5 nm) images of (a,b) M-NC, (c,d) FM-NC, (e,f) CM-NC, (g,h) CFM-NC-700, and (i,j) CFM-NC-900.
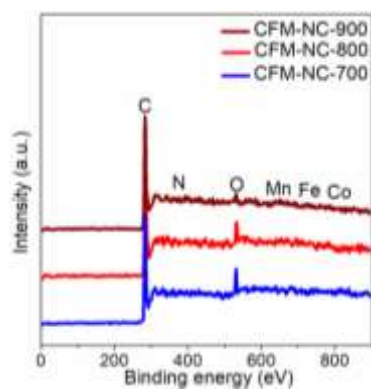
Figure S6. XPS spectra of CFM-NC-T.
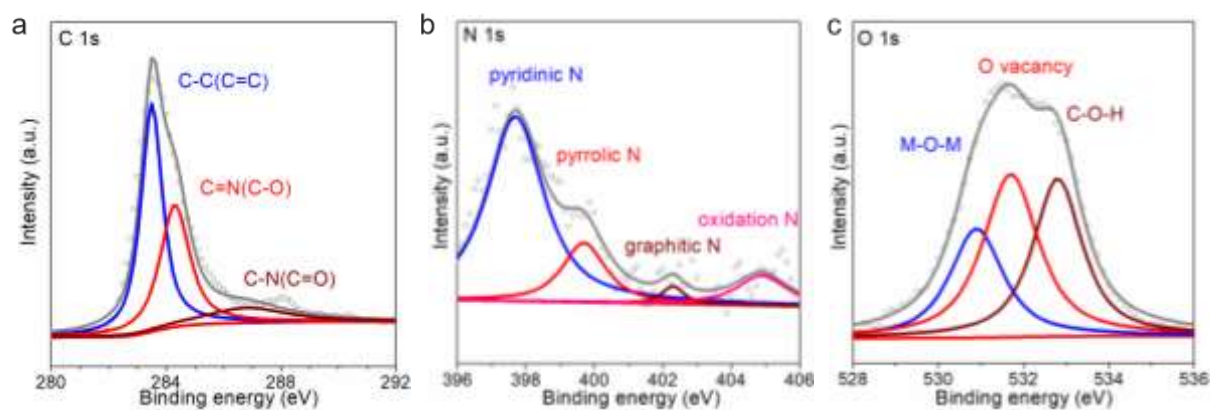
Figure S7. The high-resolution C 1s (a), N 1s (b), O 1s (c) XPS spectra of CFM-NC-700.
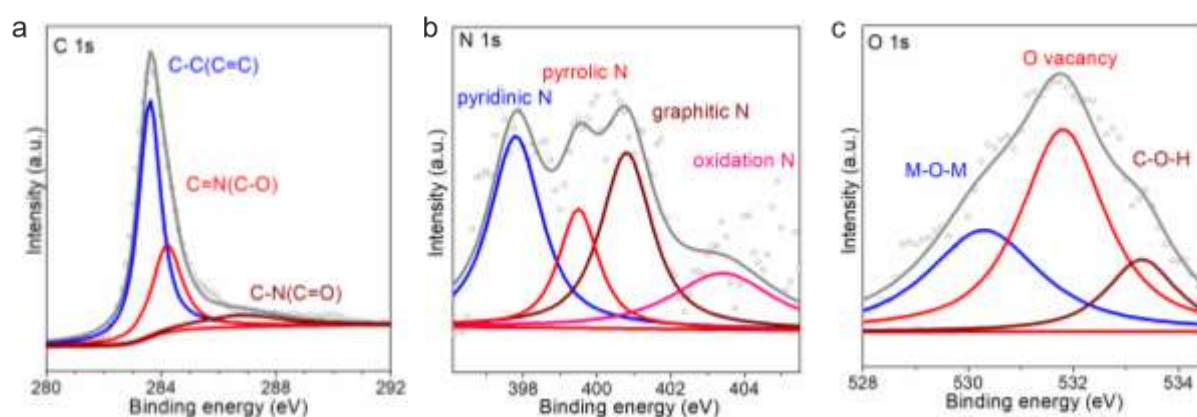
Figure S8. The high-resolution C 1s (a), N 1s (b), O 1s (c) XPS spectra of CFM-NC-900.
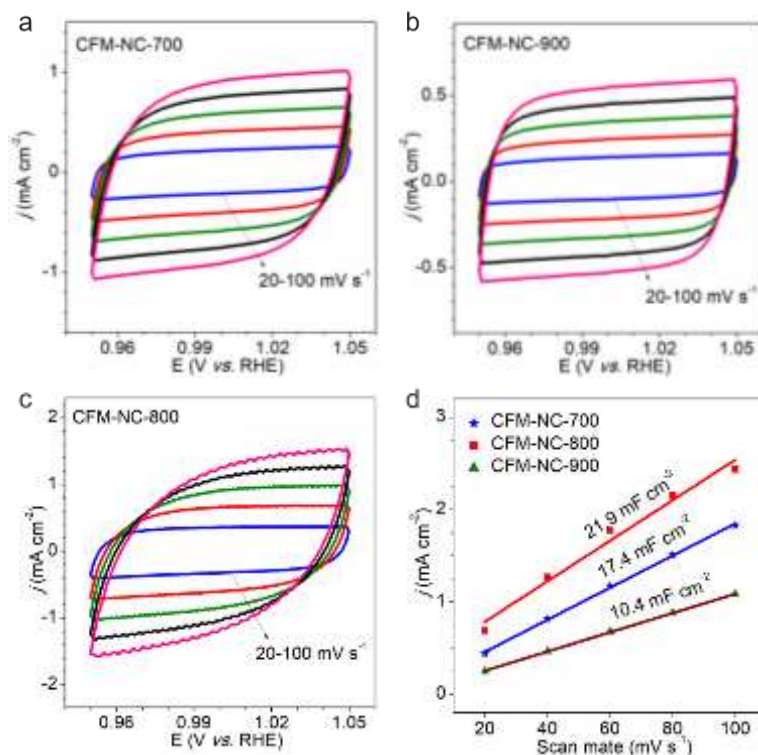
Figure S9. CVs for CFM-NC-700 (a), CFM-NC-800 (b), and CFM-NC-900 (c) in the region of 0.95-1.05 V vs RHE. (d) The C_{dl} measured by taking CV at different scan rates.

MnO   *OOH@MnO   *O@ MnO   *OH@ MnO

Figure S10. Structures of oxygen intermediates (*OOH, *O and *OH) adsorbed on MnO model (atoms colored by blue, yellow, purple, red and white represent Mn, O and H atoms, respectively).
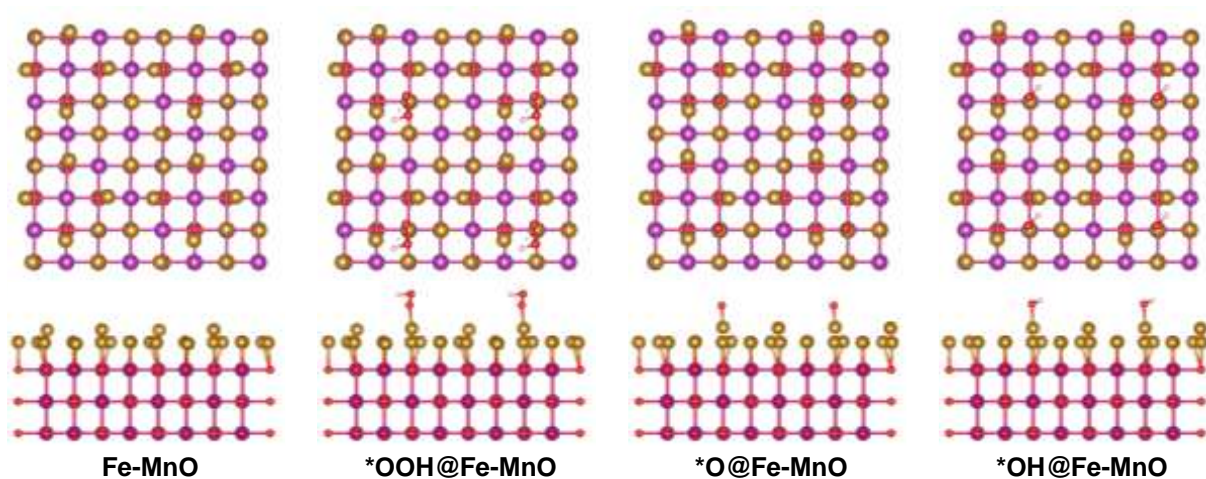
Figure S11. Structures of oxygen intermediates (*OOH, *O and *OH) adsorbed on Fe-MnO model (atoms colored by blue, yellow, purple, red and white represent Fe, Mn, O and H atoms, respectively).

Figure S12. Structures of oxygen intermediates (*OOH, *O and *OH) adsorbed on Co-MnO model (atoms colored by blue, yellow, purple, red and white represent Co, Mn, O and H atoms, respectively).

CoFe-MnO   ***OOH@CoFe-MnO***   ***O@CoFe-MnO***   ***OH@CoFe-MnO***
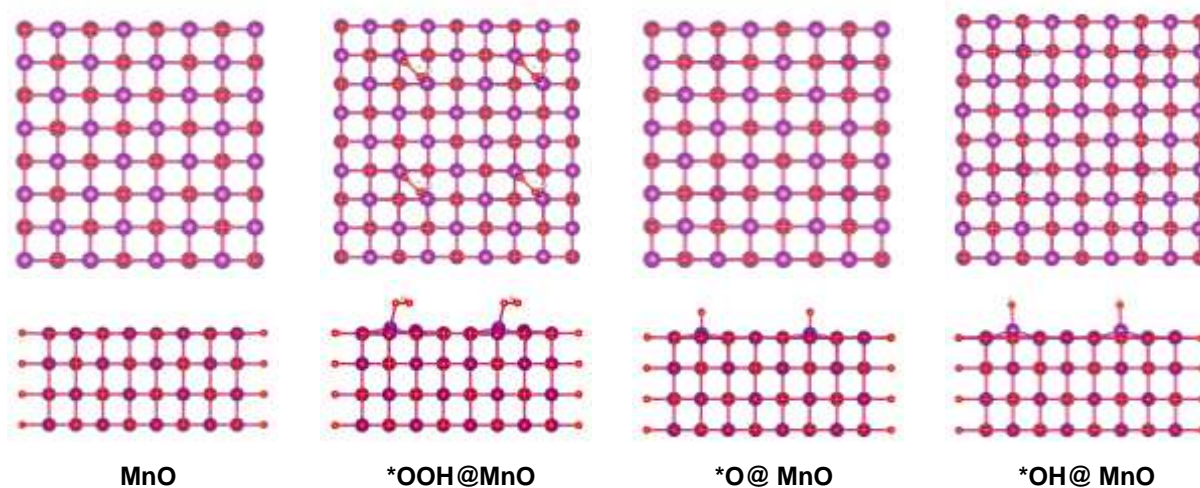
Figure S13. Structures of oxygen intermediates (*OOH, *O and *OH) adsorbed on CoFe-MnO model (atoms colored by blue, yellow, purple, red and white represent Co, Fe, Mn, O and H atoms, respectively).

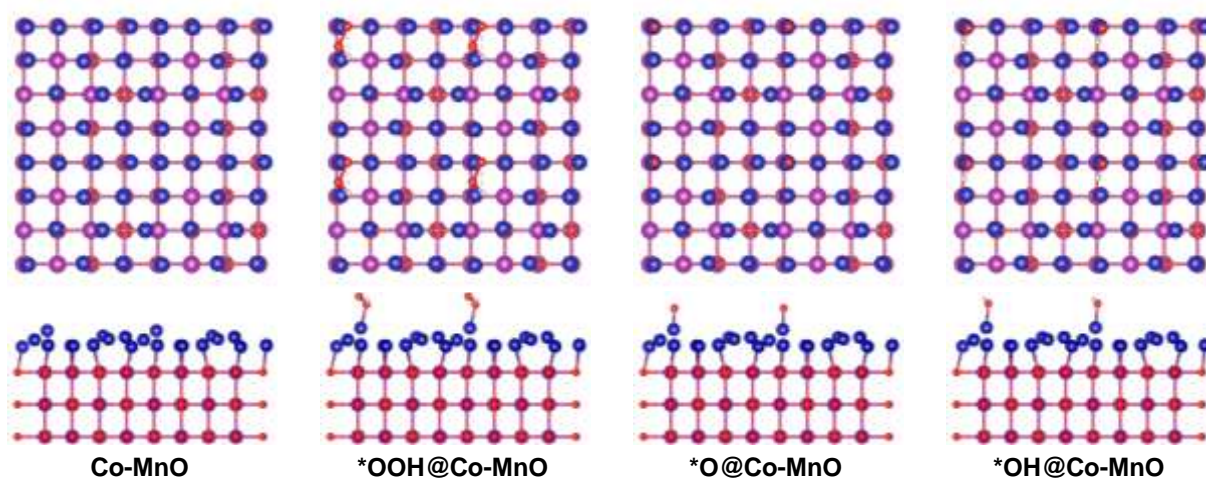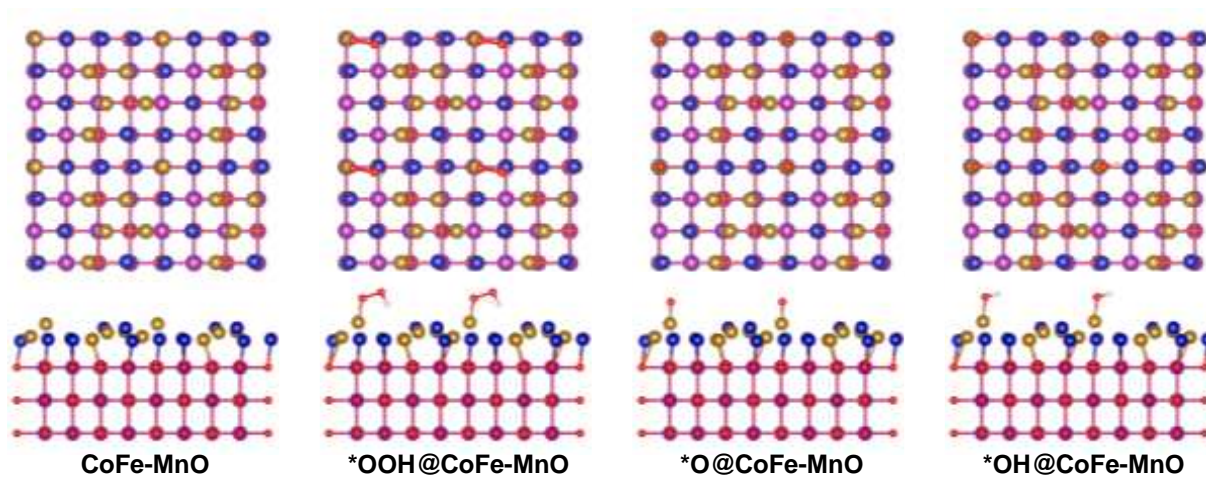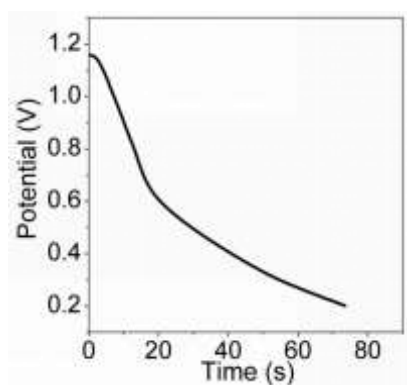**Figure S14.** Discharging curve of the primary ZAB catalyzed by pure Ni foam with an increasing current density of 1 mA cm^{-3}.
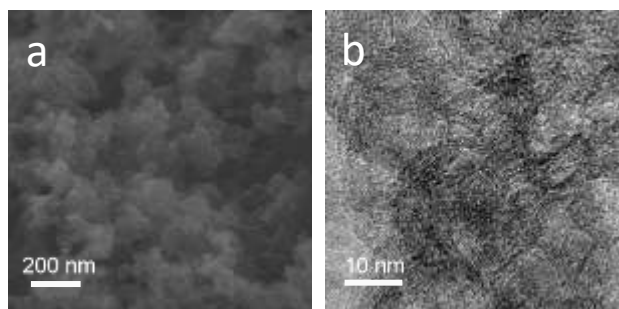
Figure S15. SEM (a) and TEM (b) images of CFM-NC-800 in the rechargeable Zn-air batteries after 80 h.

Table S1. Selected bond lengths (Å) and angles (º) for Mn-MOF.

	Mn-MOF		
Mn(1)-O(1)#1	2.179(3)	Mn(1)-O(1)	2.179(3)
Mn(1)-N(4)#1	2.193(3)	Mn(1)-N(4)	2.193(3)
Mn(1)-O(2)#1	2.223(4)	Mn(1)-O(2)	2.223(4)
O(1)#1-Mn(1)-O(1)	180.00(11)	O(1)#1-Mn(1)-N(4)#1	89.98(12)
O(1)-Mn(1)-N(4)#1	90.02(12)	O(1)#1-Mn(1)-N(4)	90.02(12)
O(1)-Mn(1)-N(4)	89.98(12)	N(4)#1-Mn(1)-N(4)	180.00(3)
O(1)#1-Mn(1)-O(2)#1	89.37(15)	O(1)-Mn(1)-O(2)#1	90.63(15)
N(4)#1-Mn(1)-O(2)#1	93.81(12)	N(4)-Mn(1)-O(2)#1	86.19(12)
O(1)#1-Mn(1)-O(2)	90.63(15)	O(1)-Mn(1)-O(2)	89.37(15)
N(4)#1-Mn(1)-O(2)	86.19(12)	N(4)-Mn(1)-O(2)	93.81(12)
O(2)#1-Mn(1)-O(2)	180.0		
Note：#1 -x,-y+1,-z			

Table S2. BET and Raman analysis for samples.

Sample	BET (m^2/g)	Raman (I_G/I_D)
M-NC	934	0.82
CM-NC	894	0.84
FM-NC	565	0.87
CFM-NC-700	809	0.87
CFM-NC-800	662	0.88
CFM-NC-900	837	0.95

Table S3. XPS spectra analysis for CFM-NC-*T* samples.

Sample	C1s (%)	N1s (%)	O1s (%)	Mn2p (%)
CFM-NC-700	87.9	2.1	9.4	0.6
CFM-NC-800	90.2	2.5	6.7	0.6
CFM-NC-900	95.3	1.2	2.9	0.6

Table S4. XPS spectra analysis for CFM-NC-*T* samples of N 1s signal.

Sample	Pyridinic-N	Pyrrolic-N	Graphitic-N	oxidized-N
CFM-NC-700	397.7 eV, 70.2%	399.7 eV, 17.1%	402.3 eV, 2.6%	404.9 eV, 10.1%
CFM-NC-800	397.7 eV, 44.5%	399.4 eV, 20.5%	401.1 eV, 10.9%	403.4 eV, 24.1%
CFM-NC-900	397.8 eV, 33.7%	399.5 eV, 16.1%	400.8 eV, 30.6%	403.4 eV, 19.6%

Table S5. Comparison of the electrocatalytic activities of CFM-NC-800 with some representative Mn-based ORR electrocatalysts reported in 0.1 M KOH solution.

Catalysts	$E_{1/2}$ (V)	Tafel slope (mV dec^{-1})	Ref.
CFM-NC-800	**0.86**	**87**	**This work**
MnO_2/C	0.79	N.A.	[2]
A-MnO_2	0.75	105	[3]
Mn_3O_4 NWs/GN/CNTs	0.84	101	[4]
MnO@Co-N/C	0.83	78	[5]
Mn/C-NO	0.86	N.A.	[6]
MnO_x/S-GC	0.82	81	[7]
Mn_3O_4/N-graphene	0.69	N.A.	[8]
N-carbon-MnO	0.76	N.A.	[9]
Ni-MnO/rGO aerogel	0.78	85	[10]
Mn_xO_y-NC	0.81	N.A.	[11]

Table S6. The performance of liquid rechargeable Zn-air batteries with various ORR electrocatalysts reported in literature.

Catalyst	Specific capacity (mAh g_{Zn}^{-1})	Peak power density (mW cm^{-2})	Ref.
CFM-NC-800	**812@10 mA cm^{-2}**	**260**	**This work**
NiFe/NCNT	772@10 mA cm^{-2}	300.7	[12]
3DOMCo@TiO$_x$N$_y$	697@20 mA cm^{-2}	110	[13]
CoFe/NGCT	748@20 mA cm^{-2}	203	[14]
CoSx/CoNC-800	770@10 mA cm^{-2}	103	[15]
Co$_9$S$_8$/NSG	655@5 mA cm^{-2}	72.1	[16]
NiFe@NCFs	719@5 mA cm^{-2}	102	[17]
NCS	636@10 mA cm^{-2}	160	[18]
CoO-NSC-900	714@10 mA cm^{-2}	65	[19]
MPZ-CC@CNT	860@25 mA cm^{-2}	162	[20]

Reference

1   J. Nørskov, J. Rossmeisl, A. Logadottir, L. Lindqvist, J. Kitchin, T. Bligaard, H. Jonsson, *J. Phys. Chem. B*, 2004, **108**, 17886.

2   J.X. Zhang, L.N. Zhou, J. Cheng, X. Yin, W.T. Kuang, Y.J. Li, *J. Mater. Chem.* A, 2019, **7**, 4699.

3   M. Jiang, C.P. Fu, J. Yang, Q. Liu, J. Zhang, B.D. Sun, *Energy Storage Materials*, 2018, **18**, 34.

4   C.S. Li, Y. Sun, W.H. Lai, J.Z. Wang, S.L. Chou, *ACS Appl. Mater. Interfaces*, 2016, **8**, 27710.

5   Y.N. Chen, Y.B. Guo, H.J. Cui, Z.J. Xie, X. Zhang, J.P. Wei, Z. Zhou, *J. Mater. Chem. A*, 2018, **6**, 9716.

6   Y. Yang, K.T. Mao, S.Q. Gao, H. Huang, G.L. Xia, Z.Y. Lin, P. Jiang, C.L. Wang, H. Wang, Q.W. Chen, *Adv. Mater.*, 2018, **30**, 1801732.

7   Y. Gao, H. Zhao, D.J. Chen, C. Chen, F. Ciucci, *Carbon*, 2015, **94**, 1028.

8   J.J. Duan, S. Chen, S. Dai, S.Z. Qiao, *Adv. Funct. Mater.*, 2014, **24**, 2072.

9   Y.H. Wang, X. Ding, F. Wang, J.Q. Li, S.Y. Song, H.J. Zhang, *Chem. Sci.*, 2016, **7**, 4284.

10 G.T. Fu, X.X. Yan, Y.F. Chen, L. Xu, D.M. Sun, J.-M. Lee, Y.W. Tang, *Adv. Mater.*, 2018, **30**, 1704609.

11 J. Masa, W. Xia, I. Sinev, A.Q. Zhao, Z.Y. Sun, S. Grützke, P. Weide, M. Muhler, W. Schuhmann, *Angew. Chem. Int. Ed.*, 2014, **53**, 8508.

12 H. Lei, Z.L. Wang, F. Yang, X.Q. Huang, J.H. Liu, Y.Y. Liang, J.P. Xie, M.S.

Javed, X.H. Lu, S.Z. Tan, W.J. Mai, *Nano Energy*, 2020, **68**, 104293.

13 G.H. Liu, J.D. Li, J. Fu, G.P. Jiang, G. Lui, D. Luo, Y.P. Deng, J. Zhang, Z.P. Cano, A.P. Yu, D. Su, Z.Y. Bai, L. Yang, Z.W. Chen, *Adv. Mater.*, 2019, **31**, 1806761.

14 X. Liu, L. Wang, P. Yu, C.G. Tian, F.F. Sun, J.Y. Ma, W. Li, H.G. Fu, *Angew. Chem. Int. Ed.*, 2018, **57**, 16166-16170.

15 Q. Lu, J. Yu, X.H. Zou, K.M. Liao, P. Tan, W. Zhou, M. Ni, Z.P. Shao, *Adv. Funct. Mater.*, 2019, **29**, 1904481.

16 Q. Shao, J.Q. Liu, Q. Wu, Q. Li, H.G. Wang, Y.H. Li, Q. Duan, *Nano-Micro Lett.*, 2019, **11**, 4.

17 Y.L. Niu, X. Teng, S.Q. Gong, Z.F. Chen, *J. Mater. Chem. A*, 2020, **8**, 13725-13734.

18 P.K. Gangadharan, S.N. Bhange, N. Kabeer, R. Illathvalappil, S. Kurungot, *Nanoscale Adv.*, 2019, **1**, 3243–3251.

19 S. Chen, S. Chen, B.H. Zhang, J.T. Zhang, *ACS Appl. Mater. Interfaces*, 2019, **11**, 16720-16728.

20 Y. Jiang, Y.P. Deng, R.L. Liang, J. Fu, D. Luo, G.H. Liu, J.D. Li, Z. Zhang, Y.F. Hu, Z.W. Chen, *Adv. Energy Mater.*, 2019, **9**, 1900911.